2020-08-03

SedimentInduced Stratification in an Estuarine Bottom Boundary Layer

Egan, G

Key Points:
- We measured sediment and flow statistics from 0–1.5 cm above a cohesive sediment bed
- Sediment-induced stratification reduced bottom drag and near-bed momentum fluxes
- A new nondimensional parameter is proposed to quantify sediment-induced stratification

Sediment-Induced Stratification in an Estuarine Bottom Boundary Layer

Galen Egan[1] , **Andrew J. Manning[1,2,3]** , **Grace Chang[4]** , **Oliver Fringer[1]** , and **Stephen Monismith[1]**

[1]Department of Civil and Environmental Engineering, Stanford University, Stanford, CA, USA, [2]HR Wallingford, Wallingford, UK, [3]School of Biological and Marine Sciences, University of Plymouth, Drake Circus, Plymouth, UK, [4]Integral Consulting Inc., Santa Cruz, CA, USA

Abstract We took field observations on the shallow shoals of South San Francisco Bay to examine how sediment-induced stratification affects the mean flow and mixing of momentum and sediment throughout the water column. A Vectrino Profiler measured near-bed velocity and suspended sediment concentration profiles, which we used to calculate profiles of turbulent sediment and momentum fluxes. Additional turbulence statistics were calculated using data from acoustic Doppler velocimeters placed throughout the water column. Results showed that sediment-induced stratification, which was set up by strong near-bed wave shear, can reduce the frictional bottom drag felt by the mean flow. Measured turbulence statistics suggest that this drag reduction is caused by stratification suppressing near-bed turbulent fluxes and reducing turbulent kinetic energy dissipation. Turbulent sediment fluxes, however, were not shown to be limited by sediment-induced stratification. Finally, we compared our results to a common model parameterization which characterizes stratification through a stability parameter modification to the turbulent eddy viscosity and suggest a new nondimensional parameter that may be better suited to represent stratification when modeling oscillatory boundary layer flows.

Plain Language Summary In estuaries, mud is eroded through the combined effect of waves and currents exerting stress on the bed. Because the mud particles are denser than water, they tend to settle downward and form thin layers of high-mud-concentration fluid near the bed. This is called sediment-induced stratification. We measured sediment concentrations and flow properties near the bed in a shallow area of South San Francisco Bay to determine how sediment-induced stratification affected the interactions between waves, currents, and mud. We found that sediment-induced stratification can make the bed feel smoother by damping turbulence. These results are important for understanding and modeling how sediment moves around in estuaries.

1. Introduction

In sediment-laden flows, the balance between vertical turbulent mixing and particle settling often induces strong gradients in suspended sediment concentration (SSC) above the bed (Nielsen, 1992). SSC gradients lead to density gradients because SSC is coupled to the fluid density through an equation of state. The result of this coupling is sediment-induced stratification, a feedback effect that increases mean shear above the stratified layer (Manning et al., 2006; Villaret & Trowbridge, 1991), reduces bottom drag (Li, 2000), and inhibits vertical turbulent transport of momentum and sediment near the bed (Glenn & Grant, 1987; Smith & McLean, 1977). This is often termed "self-regulation" or "self-stratification" (Balachandar, Cantero, Cantelli, et al., 2009a; Balachandar, Cantero, Cantelli, et al., 2009b) because the eroded sediment ultimately regulates further erosion by suppressing near-bed turbulence.

Sediment-induced stratification has been studied numerically and in both laboratory and field experiments. Direct numerical simulations of turbulent, sediment-laden, open channel flow showed that the near-bed flow relaminarized with increased near-bed SSC gradients, leading to reduced near-bed flow velocities and turbulent fluxes (Cantero, Balachandar, & Parker, 2009). In a purely oscillatory sediment-laden flow (i.e., with no mean currents), numerical simulations have also found that the flow can relaminarize (Ozdemir et al., 2010). Depending on the SSC (effects were noticeable starting at $\mathcal{O}(1-10)$ g L^{-1}), this relaminarization may occur for the entire wave cycle, during part of it, or not at all. Laboratory studies have

determined that sediment-induced stratification can reduce turbulent kinetic energy (TKE) and Reynolds stresses compared to flow over a nonerodable bed (Hooshmand et al., 2015). These effects have also been noted in the field (Friedrichs et al., 2000; MacVean & Lacy, 2014), with measured gradient Richardson numbers larger than the canonical value of 0.25 required to suppress vertical turbulent mixing in stratified shear flows (Miles, 1961).

Despite a strong conceptual understanding of sediment-induced stratification, the millimeter scales over which it acts in the field have historically presented difficulties in measuring its effects in situ. In order to more explicitly quantify the magnitude and impacts of sediment-induced stratification, we deployed acoustic instrumentation directly above an estuarine cohesive sediment bed in a shallow, wave- and current-driven flow to elucidate how stratification affects the mean and turbulent characteristics of the bottom boundary layer.

2. Field Deployment

As part of a larger study examining cohesive sediment flocculation and boundary layer dynamics, we conducted field work on the shallow (1.5-m mean lower low water, 2-m tidal range), eastern shoals of South San Francisco Bay. A comprehensive description of the site conditions, including a site map, wind and tide strength, sediment bed characteristics and variability, and hydrodynamics instrumentation that we deployed can be found in our previous paper (Egan et al., 2019), which focused on the bottom boundary layer shear stress dynamics without consideration of sediment-induced stratification. For completeness, the most pertinent background information from that work will be summarized here and in section 3.

Instruments on a single platform collected data from 17 July 2018 to 2 August 2018. The platform contained three acoustic Doppler velocimeters (ADVs; Nortek USA, Boston, MA) placed with their measurement volumes at 5, 15, and 45 cm above the bed (cmab). Each ADV sampled the pressure, 3-D velocity, and acoustic backscatter at 8 Hz for 14 min each hour. The platform also held a Nortek Vectrino Profiler (Vectrino) deployed with its measurement volume overlapping the bed such that it reported the 3-D velocity and acoustic backscatter over 1 mm-spaced vertical bins from 0–1.5 cmab at 64 Hz for 12 min each hour. This gave approximately 46,000 data points for analysis in each vertical bin during each burst period. On the same platform, we deployed an upward facing Nortek Aquadopp Acoustic Doppler Current Profiler (ADCP), which reported mean current profiles over 0.1 m vertical bins every 3 min based on 72 s of sampling.

Approximately 30 m from the main platform, we deployed an auxiliary optical sensing platform containing a Sequoia Scientific, Inc. (Bellevue, WA) LISST-100x (LISST; Laser In Situ Scattering and Transmissometry) with its measurement volume at 15 cmab. The LISST collected 60-s burst-averaged suspended sediment particle size distributions (PSDs) each hour during the middle of the Vectrino burst period (Agrawal & Pottsmith, 1994). We also collected two box cores from the sediment bed to determine sediment bed properties and collected water samples for in situ floc cam measurements of particle size and settling velocity.

3. Methods

3.1. Sediment Data

Vectrino and ADV acoustic backscatter were calibrated against water samples containing varying sediment mass concentrations (10–10,240 mg L^{-1} for the Vectrino and 1–1,280 mg L^{-1} for the ADVs). The mud used in the calibration was collected from the bed near our study site using a Ponar grab sampler and added to water to produce the desired SSC. This allowed us to obtain time series estimates of SSC over the Vectrino profile and at each ADV sampling height. For the Vectrino calibration, we time-averaged the beam amplitudes over a 2-min burst and plotted the resulting amplitude against the log of the measured SSC. This procedure was performed for each vertical bin (assuming that the SSC was identical in each bin) because the Vectrino backscatter amplitude varies parabolically over its profile due to probe geometry-induced SNR variations (Thomas et al., 2017). Figure 1a shows the result of this calibration, though for clarity only the vertically averaged amplitude is plotted. The fit was excellent for each individual vertical bin ($0.94 \leq r^2 \leq 0.99$). A similar procedure was used for the ADV data, though we did not need to vertically average because the ADVs provide a point measurement. The ADV calibration curves are shown in Figure 1b.
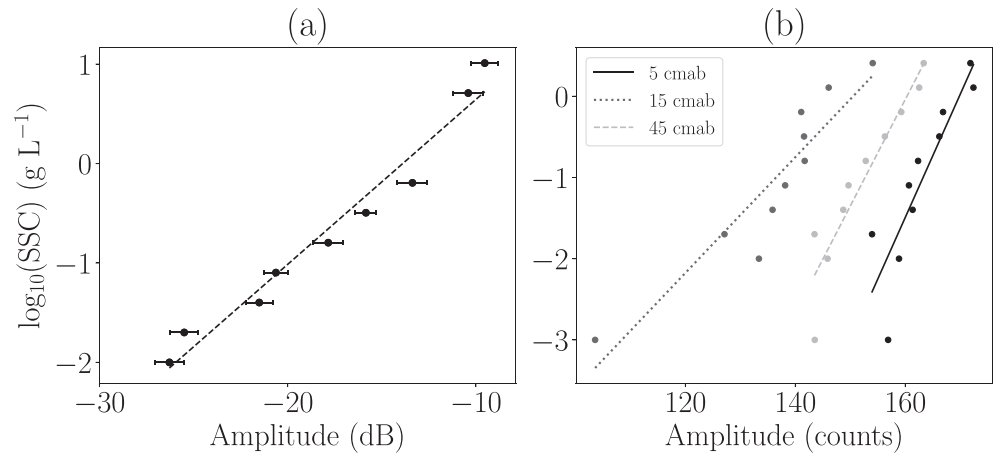
Figure 1. (a) Vertically averaged backscatter to SSC calibration for the Vectrino Profiler, with $r^2 = 0.96$. Error bars denote the standard error around the vertically averaged backscatter amplitude. (b) Backscatter to SSC calibration for the ADVs at 5 cmab ($r^2 = 0.79$), 15 cmab ($r^2 = 0.86$), and 45 cmab ($r^2 = 0.89$).

The acoustic backscatter-SSC relationships were approximately log-linear in the observed range as expected (Lohrmann, 2001), indicating that the acoustic backscatter readings can serve as a reliable indicator of relative SSC changes at each individual instrument. We avoid interinstrument SSC comparisons because variations in particle size and acoustic pulse transmit power among the different instruments were not accounted for and can have a confounding effect on the calibrations (Lohrmann, 2001).

The magnitude of vertical density stratification was quantified with the Brunt-Väisälä (or buoyancy) frequency, N, defined as

$$N = \sqrt{-\frac{g}{\rho_0}\frac{\partial\bar{\rho}}{\partial z}}, \tag{1}$$

where g is acceleration due to gravity, ρ_0 is the background fluid density (assumed a constant $\rho_0 = 1,020$ kg m^{-3}), and z is the vertical coordinate. The time-averaged fluid density, $\bar{\rho}$, and its vertical gradient were calculated from the SSC data derived from the Vectrino calibrated acoustic backscatter amplitude. The measured SSC (mass concentration) is the excess density to the bulk mixture, so the total fluid density is given by

$$\bar{\rho} = \rho_0 + \bar{c}. \tag{2}$$

Here, $\bar{c}$ is the burst-averaged SSC. Implicit in Equation 2 is the assumption that the fluid density in the Vectrino measurement volume was only affected by changes in SSC. Because turbulence is strong near the bed and the profile is only calculated over 1.5 cm, it is likely reasonable to assume that salinity and temperature stratification are negligible in that region. Therefore, while the background density may have changed slightly over the deployment period, the vertical density gradient was primarily controlled by the SSC profile.

To estimate the particle settling velocity, we assumed Stokes settling (Stokes, 1851),

$$w_s = \frac{(\rho_s - \rho_0)g d_p^2}{18\mu}, \tag{3}$$

where ρ_s is the sediment density, w_s is the floc settling velocity, d_p is the particle diameter representative of the average floc size, and μ is the dynamic viscosity of water. Equation 3 was used to determine w_s for each Vectrino burst period, assuming a constant effective density of $(\rho_s - \rho_0) = 280$ kg m^{-3} and a particle diameter $d_p = d_{50}$, the median diameter determined from the LISST PSDs. Over the deployment period, the average PSD standard deviation was 8.5 μm, so while d_{50} alone did not capture the settling dynamics of

the entire sediment population, it was an adequate representation of the burst-to-burst variability. The effective density was estimated based on laboratory bulk density measurements performed on the sediment cores. This gave values that were consistent with In Situ Settling Velocity LabSFLOC (INSSEV-LF) floc cam video system measurements (Manning et al., 2007) taken the day after platform deployment, which determined an average effective density of 299 kg m^{-3} with a standard deviation of 353 kg m^{-3}, calculated from 180 individual flocs with effective densities ranging from 13 to 1,856 kg m^{-3}. The INSSEV-LF simultaneously measures particle diameter and settling velocity, allowing for direct estimation of $(\rho_s - \rho_0)$ after rearranging Equation 3.

The sediment cores that we collected were also used for a laboratory erosion study using a U.S. Environmental Protection Agency (USEPA) certified Sediment Erosion with Depth flume (SEDflume) (McNeil et al., 1996). The SEDflume measures the sediment erosion rate as a function of applied shear stress, allowing for determination of both critical shear stress and erosion rates with depth.

3.2. Hydrodynamics Data

Hydrodynamics data were processed in the same manner as described in our previous paper (Egan et al., 2019), but we will summarize the derived variables here for clarity. Velocity data were rotated into major and minor directions, denoted u and v, respectively, corresponding to the first and second principal components of the ADCP mean velocity over the 16-day deployment period. The vertical velocity is denoted w. Velocity measurements time-averaged over a measurement burst period are denoted $\bar{u}$, turbulent fluctuations from the average are denoted u', and wave-induced fluctuations are denoted $\tilde{u}$. For each measurement burst period, we calculated the turbulent Reynolds stress, $\overline{u'w'}$, for both the ADV and Vectrino data. We also calculated the wave momentum flux, $\overline{\tilde{u}\tilde{w}}$, and the TKE dissipation rate, ϵ. Using the calibrations shown in Figure 1, the turbulent sediment flux, $\overline{c'w'}$, was estimated for both the Vectrino and ADV data using the phase method (Bricker & Monismith, 2007).

We estimated a drag coefficient from our data with

$$C_D = \left(\frac{u_*}{u_r}\right)^2, \tag{4}$$

where u_* is the friction velocity and u_r is a reference velocity, which was taken as the mean velocity at a reference height $z_r = 1.2$ cmab as measured by the Vectrino. The friction velocity was estimated as

$$u_* = \left| \nu \frac{\partial \bar{u}}{\partial z} - \overline{u'w'} \right|_b^{1/2}, \tag{5}$$

where ν is the kinematic viscosity of water, $\frac{\partial \bar{u}}{\partial z}$ is the vertical gradient of the horizontal velocity estimated from the Vectrino mean velocity data, and the subscript b indicates a bottom measurement. The bed at our study site was characterized by a 4–5-mm thick canopy of biological roughness elements where SSC remained elevated from wave-induced resuspension, but the mean flow was suppressed (see Figure 2). Therefore, consistent with the turbulence statistics in our previous work (Egan et al., 2019), we defined bottom measurements as corresponding to 1 mm (i.e., one Vectrino measurement bin) above the top of the canopy elements. This renders Equation 5 a direct measurement of the bed shear stress induced by the mean flow.

Wave statistics were also estimated from Vectrino data, in particular the wave frequency, ω, and the bottom wave-orbital velocity, u_b. From u_b, we can estimate a wave shear stress, defined as

$$\tau_w = \frac{1}{2} \rho_0 f_w u_b^2, \tag{6}$$

where f_w is the wave friction factor (Jonsson, 1967). The specific formulation for f_w depends on whether the wave boundary layer is laminar or turbulent. Precise cutoffs for turbulence have been determined by laboratory studies (Jonsson, 1967; Kamphuis, 1975) and vary in $\frac{a_b^2 \omega}{\nu} - \frac{k_b}{a_b}$ space, where k_b is the physical
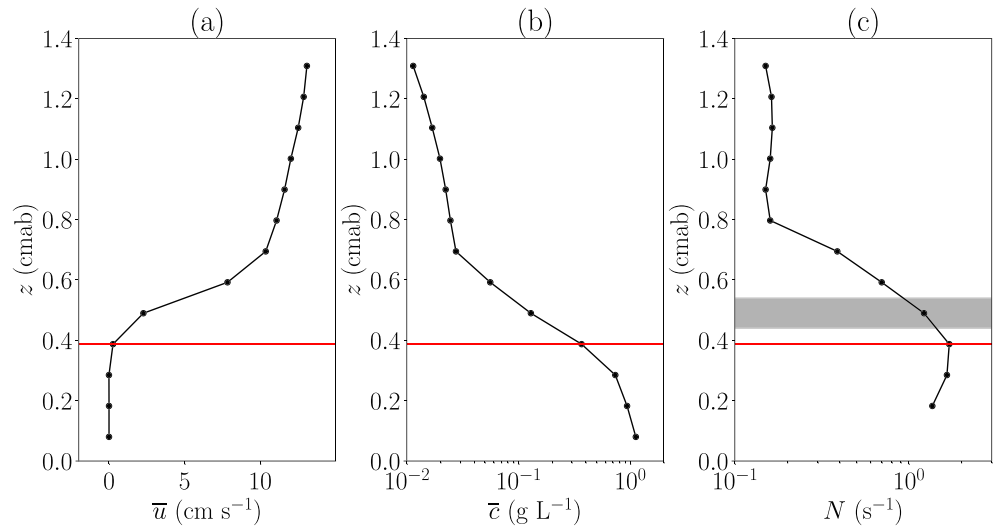
Figure 2. (a) Mean velocity profile in the major current direction measured by the Vectrino, (b) mean SSC profile measured by the Vectrino, and (c) buoyancy frequency N calculated from Vectrino data using Equation 1. The solid red line indicates the kink point in the velocity profile at the top of the biological canopy covering the bed, and the gray shading in panel (c) indicates the bin at which all reported values of N are measured.

bottom roughness and $a_b = u_b\omega^{-1}$ is the bottom wave-orbital excursion amplitude (Lacy & MacVean, 2016). Using a value of $k_b = 1$ cm, we found that the wave boundary layer was predominantly in the turbulent regime. Therefore, following Nielsen (1992), the wave friction factor is given by

$$f_w = \exp\left(5.213\left(\frac{k_b}{a_b}\right)^{0.194} - 5.977\right). \tag{7}$$

Throughout this paper we will examine various hydrodynamic quantities as a function of nondimensional wave strength. For this purpose we chose the wave Reynolds number, defined as

$$Re_\delta = \frac{u_b\delta_w}{\nu}, \tag{8}$$

where $\delta_w = \sqrt{2\nu\omega^{-1}}$ is the Stokes wave boundary layer thickness.

3.3. Model Comparison

Field-scale sediment transport models cannot resolve stratification dynamics within the millimeter-scale wave boundary layer. Therefore, they rely on parameterizations to represent the suppression of near-bed turbulence by sediment-induced stratification. Our data set presents a unique opportunity to test and validate these parameterizations. The most widely used model is that proposed by Styles and Glenn (2000) (hereafter SG2000), which represents stratification effects through a modification to the eddy viscosity,

$$K_{strat} = \frac{K}{1 + \beta\frac{z}{L}}, \tag{9}$$

where K_{strat} is the stratified eddy viscosity, K is the unstratified (or neutral) eddy viscosity, $\beta = 4.7$ is an empirical constant, and $\frac{z}{L}$ is the stability parameter, which is estimated in the wave boundary layer with

$$\frac{z}{L} = \frac{K}{u_{*cw,sg}^4}g(s-1)w_s\bar{c}. \tag{10}$$

Here, $u_{*cw,sg}$ is the combined wave-current friction velocity calculated with the SG2000 model, $s = \rho_s\rho_0^{-1}$ is the relative density, and we have assumed that the vertical turbulent sediment flux (parameterized through a
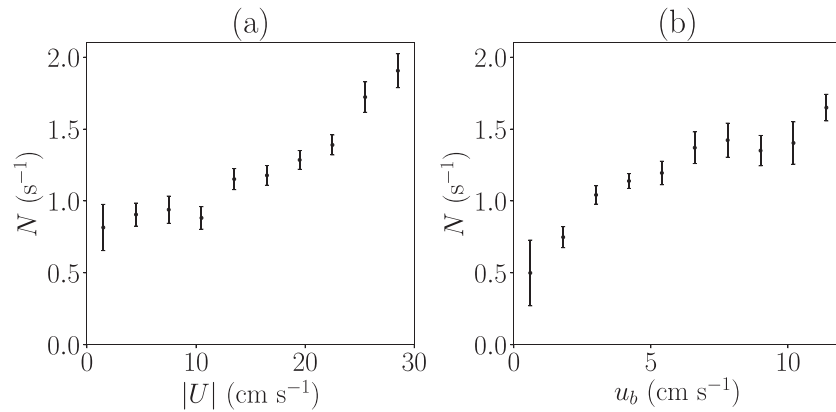
Figure 3. The buoyancy frequency, N, as a function of (a) $|U|$, the depth-averaged current magnitude, and (b) u_b, the bottom wave-orbital velocity.

sediment diffusivity, κ_s) is in balance with the settling flux, that is, $\kappa_s \frac{\partial \bar{c}}{\partial z} = w_s \bar{c}$. To calculate the stability parameter for our data, we used our LISST measurements and Stokes settling (Equation 3) to estimate w_s, the Vectrino backscatter to estimate $\bar{c}$, and SG2000 to estimate K and $u_{*cw,sg}$.

In section 4.6, we will examine how our measured eddy viscosity, K_{meas}, evolves with various metrics for stratification, including the stability parameter given in Equation 10. There are, however, multiple methods to estimate the eddy viscosity. For consistency with SG2000, we assume a linear eddy viscosity of the form

$$K_{meas} = \kappa z u_{*cw},$$
(11)

where u_{*cw} is the combined wave-current friction velocity measured by the Vectrino, defined as

$$u_{*cw} = \left| \nu \frac{\partial \bar{u}}{\partial z} - \overline{u'w'} - \overline{\tilde{u}\tilde{w}} \right|_b^{1/2}.$$
(12)

This follows from our definition of u_* in Equation 5, with the addition of the measured wave momentum flux to account for the wave-induced stress component. Based on our previous results (Egan et al., 2019), this is likely the most accurate representation of the full bed shear stress as it contains the viscous, turbulent, and wave components. Further, it accounts for stratification inherently because it is measured in the stratified bottom boundary layer.

4. Results and Discussion

4.1. Stratification

Figures 2a and 2b show characteristic 12-min average velocity and SSC profiles, respectively, and Figure 2c shows N calculated from Equation 1 for the same burst period. Here, the bed is located at $z = 0$ and is determined by the Vectrino boundary-finding algorithm (Craig et al., 2011). A canopy of biological material at the bed resulted in suppressed mean velocities and turbulence along with high SSC and N in a 4 mm-thick region above the bed, as seen below the solid red line in Figure 2. The gray shading in Figure 2c shows the bin 1 mm above the canopy top, which is the location of all values of N and all of the Vectrino turbulence statistics reported in this paper.

Stratification is often characterized across a range of hydrodynamic conditions using the gradient Richardson number,

$$\text{Ri}_g = \frac{N^2}{S^2},$$
(13)

where $S^2 = \left(\frac{\partial \bar{u}}{\partial z}\right)^2 + \left(\frac{\partial \bar{v}}{\partial z}\right)^2$ is the squared mean shear. The gradient Richardson number, however, is

inversely correlated to the mean current magnitude, making it difficult to discern the precise relationship between the mean currents and the setup of near-bed concentration gradients (this point will be elaborated on in section 4.2). Therefore, we show N, rather than Ri_g, bin averaged by the ADCP depth-averaged current magnitude, $|U|$, in Figure 3a. We depth-averaged over the lower 1 m of the water column to mitigate contamination from surface waves. For $|U| < 10 \, \text{cm s}^{-1}$, N remains relatively constant, indicating that the mean currents are not strong enough to erode sediment and set up near-bed concentration gradients. This trend changes near $|U| = 10 \, \text{cm s}^{-1}$, where N begins to increase. The sudden onset of near-bed concentration gradients at a particular current strength is suggestive of a critical shear stress for erosion, the basis of nearly all cohesive sediment erosion parameterizations (e.g., Mehta & Partheniades, 1982; Sanford & Maa, 2001).

Figure 3b shows N bin averaged by the bottom wave-orbital velocity, u_b. Unlike its relationship with the mean current magnitude, N increases steadily until $u_b \approx 7.5 \, \text{cm s}^{-1}$. Thereafter, it increases more gradually. This implies that waves, even when relatively weak, are much more effective than mean currents at eroding sediment and inducing near-bed concentration gradients in shallow systems, a result that is consistent with numerous field studies of cohesive sediment erosion in San Francisco Bay (Brand et al., 2010; MacVean & Lacy, 2014) and numerical studies of cohesive sediment erosion in combined wave-current flows (Nelson & Fringer, 2018).

4.2. Nondimensional Parameters

The results in Figure 3 illustrate a fundamental complication: The wave- and current-driven sediment stratification problem is replete with feedback effects among the various physical processes. For example, bottom drag is positively correlated to wave strength in a combined wave-current flow (Grant & Madsen, 1979), but as seen in Figure 3b, these same waves can cause near-bed sediment-induced stratification, which acts to reduce bottom drag. Erosion from the bed also increases with wave and current strength, yet is capped by sediment-induced stratification, which itself is a complex function of wave and current conditions. Therefore, it is difficult to isolate the effect of stratification on the quantities of interest, namely, bottom drag, turbulence statistics, and sediment fluxes.

Most studies quantifying the stability of stratified turbulent flows (e.g., Abarbanel et al., 1984; Howard, 1961; Miles, 1961) do so through the gradient Richardson number (Equation 13). In an oscillating flow, however, the suitability of Ri_g and its critical stability threshold remains dubious because the wave-induced shear vanishes in both the mean and instantaneous sense, leading to unphysically large Ri_g. It is also problematic because in the presence of sediment-induced stratification, N is a dependent variable that is positively correlated to wave activity and is not a good measure of stratification independent of wave conditions. This is of practical concern from a modeling standpoint because field-scale sediment transport models cannot resolve the wave boundary layer. Therefore, N is generally unknown, so we cannot assume a background N upon which the mean shear acts; this contrasts with more common modeling scenarios of stratified turbulence, for example, the thermocline in the ocean (Munk, 1948), where stratification is set up by external thermal forcing.

Another problem arises when examining the drag coefficient defined in Equation 4 across the range of Ri_g, because $C_D \sim u_*^2$, while $Ri_g \sim u_*^{-2}$, leading to erroneous correlations. Therefore, it is difficult to quantify how stratification affects bottom drag using Ri_g. Ideally, a nondimensional parameter could be defined that is proportional to Ri_g that describes the state of stratification in the system based purely on independent flow and sediment variables. Despite an extensive analysis using the Buckingham Π theorem (not shown), we were unable to form a nondimensional number that was sufficiently correlated to the measured Ri_g. Therefore, we next attempted to nondimensionalize a dependent stratification parameter, N, in a way that reduced its dependence on wave strength. There were two natural choices for this: the wave frequency, ω, and a measure of the wave-induced vertical shear rate, $u_b \delta_w^{-1}$. Nondimensionalizing N by each of these and squaring the result (analogous to a Richardson number) results in a wave frequency-based Richardson number,

$$\text{Ri}_\omega = \frac{N^2}{\omega^2}, \tag{14}$$

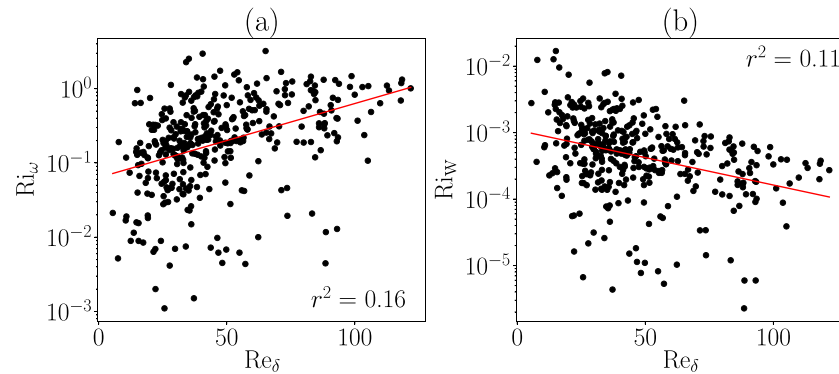and a wave shear-based Richardson number,

Figure 4. (a) The wave frequency Richardson number, Ri_ω (Equation 14), and (b) the wave shear Richardson number, Ri_W (Equation 15), as functions of the wave Reynolds number, Re_δ (Equation 8), with the red line denoting a least-squares fit.

$$\mathrm{Ri}_\mathrm{w} = \frac{N^2}{u_b^2 \delta_w^{-2}}. \tag{15}$$

Each of the above choices can be plotted against the the wave Reynolds number (Equation 8), which characterizes wave strength. Figures 4a and 4b show Ri_ω and Ri_w, respectively, as functions of Re_δ. Normalizing by the wave frequency results in a weak positive correlation ($r^2 = 0.16$ from a least squares regression) with Re_δ, whereas normalizing by $u_b^2 \delta_w^{-2}$ results in a weak negative correlation with Re_δ ($r^2 = 0.11$).

In terms of bottom drag and near-bed sediment fluxes, we expect waves and stratification to have competing effects: Waves increase drag and erosion, while stratification can limit them. Therefore, we would prefer to examine stratification through a nondimensional parameter that is slightly positively correlated to wave strength, such as Ri_ω, rather than negatively correlated, like Ri_w. For example, if bottom drag decreased with increased Ri_ω, then that decrease was likely caused by stratification *in spite of* the correlated increase in wave Reynolds number (Figure 4a), which would be expected to increase drag. Conversely, if bottom drag decreased with increased Ri_w, it would be more difficult to determine whether that drag decrease was due to stronger stratification or the correlated decrease in wave Reynolds number that accompanies increased Ri_w (Figure 4b). Therefore, in what follows, we will use Ri_ω as a measure of stratification, because it is slightly positively correlated to Re_δ.

We also needed to nondimensionalize the measured turbulence statistics. A common nondimensionalization for the turbulent Reynolds stress is the squared friction velocity, u_*^2 (Grant & Madsen, 1986). Similarly, the dissipation rate is often normalized using the unstratified turbulent open channel flow scaling, $u_*^3 (\kappa z)^{-1}$ (e.g., Feddersen et al., 2007), where $\kappa = 0.41$ is the von Kármán constant. However, using the friction velocity defined in Equation 5 is problematic because it is a function of the Reynolds stress, which is one of the quantities that we want to nondimensionalize. Therefore, we chose to replace u_* by the depth-averaged current magnitude $|U|$, resulting in normalization factors $|U|^2$ and $|U|^3 (\kappa z)^{-1}$ for the Reynolds stress and dissipation rate, respectively.

Finally, we nondimensionalized the turbulent sediment flux, $\overline{c'w'}$, using a combination of turbulence and sediment parameters. Assuming a balance between erosion and deposition near the bed, $\overline{c'w'} \sim \bar{c}_b w_s$, where $\bar{c}_b$ is the time-averaged SSC measured by the Vectrino at a measurement height of 1 mm above the canopy top. This results in a nondimensional turbulent sediment flux $\overline{c'w'}(\bar{c}_b w_s)^{-1}$. For the ADV sediment fluxes, we nondimensionalized by $\bar{c}_z w_s$, where $\bar{c}_z$ is the average concentration measured by the ADV at height z during the burst period, and w_s is the same settling velocity used in the Vectrino normalization, that is, inferred from the LISST measurements.

4.3. Mean Flow

Drag reduction is the primary impact of stratification on the mean flow. We will examine this effect by dividing our data set into two categories: low Ri_ω (weak stratification) and high Ri_ω (strong stratification), with
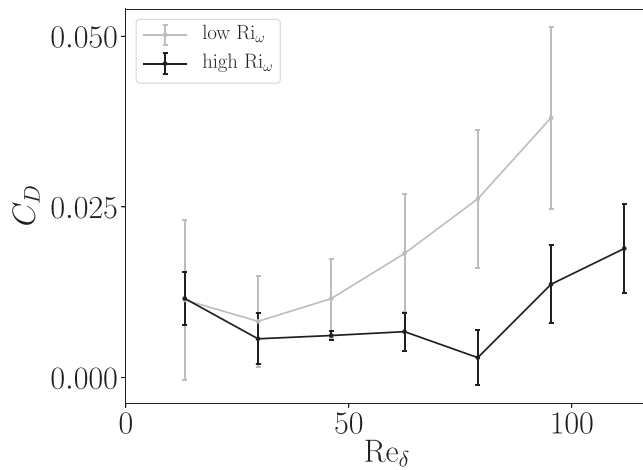
Figure 5. Drag coefficient, C_D, defined in Equation 4 for both weak stratification (gray line) and strong stratification (black line) as a function of the wave Reynolds number, Re_δ (Equation 8). Error bars denote the standard error on the bin averaging.

the cutoff determined such that there are an equal number of data points in each category. The drag coefficient, C_D (Equation 4), was then bin averaged by the wave Reynolds number, Re_δ. We then investigated the variability of C_D across the range of wave conditions in both the strong and weak stratification cases, as shown in Figure 5. For our analysis, we ignored unphysically high C_D values, quantified as three standard deviations above the median or greater, which arose during bursts when $u_r \approx 0$.

In the weak stratification case, C_D generally increases with wave strength, consistent with our previous results (Egan et al., 2019). For the strong stratification case, however, the drag increase is both smaller in magnitude and more gradual, only beginning near $Re_\delta = 80$. This indicates that near-bed stratification tends to reduce bottom drag relative to the weakly stratified case, keeping C_D relatively constant when it would otherwise increase with wave strength.

At the bin corresponding to the strongest waves where we have data for both stratification conditions, the mean drag coefficient is approximately 3 times larger in the low stratification case compared to the highly stratified case. This difference could be substantial in the context of hydrodynamic and sediment transport modeling. Most large-scale hydrodynamic models of San Francisco Bay are extremely sensitive to the choice of drag coefficient (Fong et al., 2009; Gross et al., 1999), and it is often used as a tuning parameter to match observations. These results, and those of previous field studies in the region (Bricker et al., 2005), suggest that accounting for sediment-induced stratification is critical for accurately parameterizing bottom drag and the resulting feedback effects on sediment transport.

In practice, modeling studies often neglect sediment-induced stratification effects in their bottom drag parameterizations (e.g., Chou et al., 2018; Deltares, 2019) in favor of simpler formulations. A notable exception to this is the Community Sediment Transport Modeling System (CSTMS) (Warner et al., 2008). CSTMS can estimate the bottom stress using the SG2000 model, which explicitly accounts for sediment-induced stratification. This model, however, was not formulated for cohesive sediments, nor do its assumptions about the near-bed flow structure hold over a canopy-like bed (Egan et al., 2019). We will further explore the applicability of the SG2000 stratification correction to our system in section 4.6.

4.4. Turbulence Statistics

Suppression of near-bed turbulent fluxes is the physical mechanism by which sediment-induced stratification affects the flow. Therefore, we will examine the normalized turbulent Reynolds stress and TKE dissipation rate estimated from near-bed Vectrino data for a range of stratification conditions. Neither the normalized Reynolds stress nor the normalized dissipation rate were positively correlated to wave strength, so $\overline{u'w'}|U|^{-2}$ and $\epsilon \kappa z|U|^{-3}$ are simply bin averaged by Ri_ω and plotted in Figures 6a and 6b, respectively. As with the drag coefficient, values more than three standard deviations from the median were ignored.

In general, each of the turbulence statistics decreases across the range of Ri_ω. The Reynolds stress decreases steadily by over an order of magnitude from the lowest to highest levels of stratification, while dissipation decreases by more than 2 orders of magnitude, suggesting that sediment-induced stratification can fundamentally alter the structure of near-bed turbulence by suppressing turbulent fluxes and dissipation.

We can also examine the relationship between stratification and turbulence in the ADV data. Figures 7a and 7b show the normalized Reynolds stress and TKE dissipation rate, respectively, calculated by ADVs at 5, 15, and 45 cmab. Trends are similar to those seen in the Vectrino data, with a general decrease in both Reynolds stress and dissipation rate with increasing Ri_ω.

Contrasting with the Vectrino data, ADV turbulence statistics show more sensitivity to stratification below $Ri_\omega = 0.025$ than they do beyond that point, as seen in Figure 7. We can explain this as follows: The Vectrino turbulence statistics decrease consistently with stratification because the measurements are taken within the stratified bottom boundary layer. Therefore, stronger stratification will consistently suppress turbulent
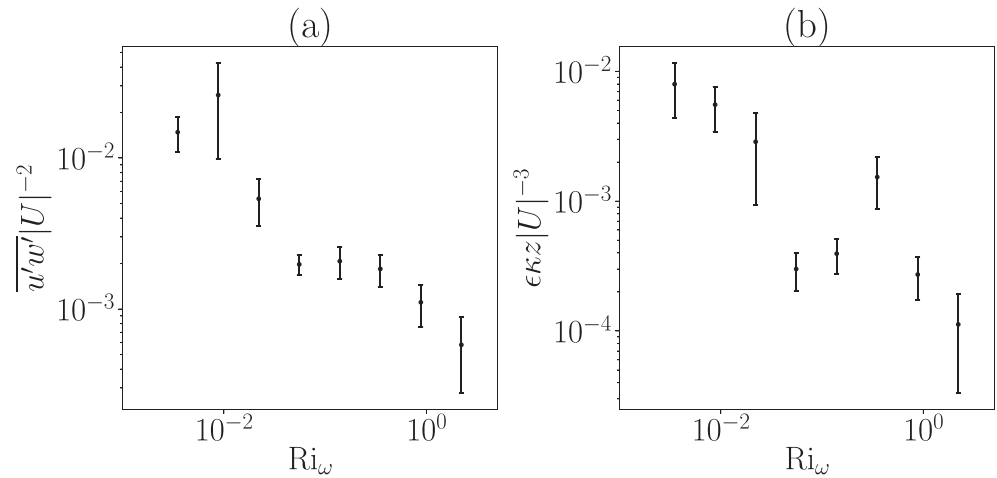
Figure 6. Turbulence statistics calculated from Vectrino data 1 mm above the canopy top and bin averaged by Ri_ω:(a) nondimensional Reynolds stress stress, $\overline{u'w'}|U|^{-2}$, and (b) TKE dissipation rate, $\epsilon\kappa z|U|^{-3}$. Error bars denote the standard error on the bin averaging.

fluctuations. Conversely, the flow is not stratified in the ADV measurement volumes; turbulent stresses and dissipation merely decrease because the near-bed stratification makes the bed feel smoother. This drag reduction can accelerate the flow outside the boundary layer, thus increasing turbulence production further from the wall and effectively balancing stratification-induced decreases in turbulent stresses and dissipation. This result agrees with direct numerical simulations of stratified wave- and current-driven flow (Nelson, 2018), where it was shown that turbulent shear production increases above the stratified bottom boundary layer. Those simulations also showed that stratification-induced decreases in the Reynolds stress were strongest near the bed and relatively small higher in the water column. Therefore, we expect that reductions in turbulence away from the bed are limited when they are solely caused by near-bed processes.

Another explanation for the increased turbulent stresses and dissipation in Figure 7 relative to Figure 6 could be proximity to the free surface. The measurement periods when stratification was strongest corresponded to periods of strong surface waves (Figure 3), presumably corresponding to higher wind stresses and wave dissipation. Therefore, the approximately constant stresses and dissipation beyond $Ri_\omega = 0.025$ in Figure 7 could be indicative of a balance between stratification suppressing turbulence and surface wind stress amplifying it.
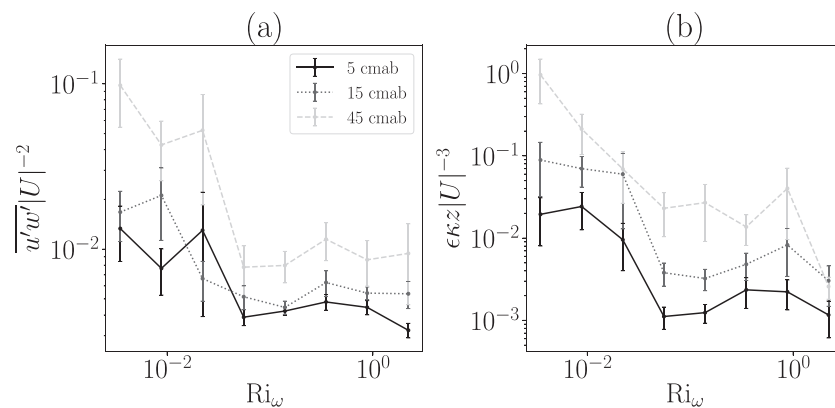

Figure 7. Turbulence statistics calculated from ADV data at 5 (black solid line), 15 (dark gray dotted line), and 45 (light gray dashed line) cmab and bin averaged by Ri_ω: (a) nondimensional Reynolds stress stress, $\overline{u'w'}|U|^{-2}$, and (b) TKE dissipation rate, $\epsilon\kappa z|U|^{-3}$. Error bars denote the standard error on the bin averaging.
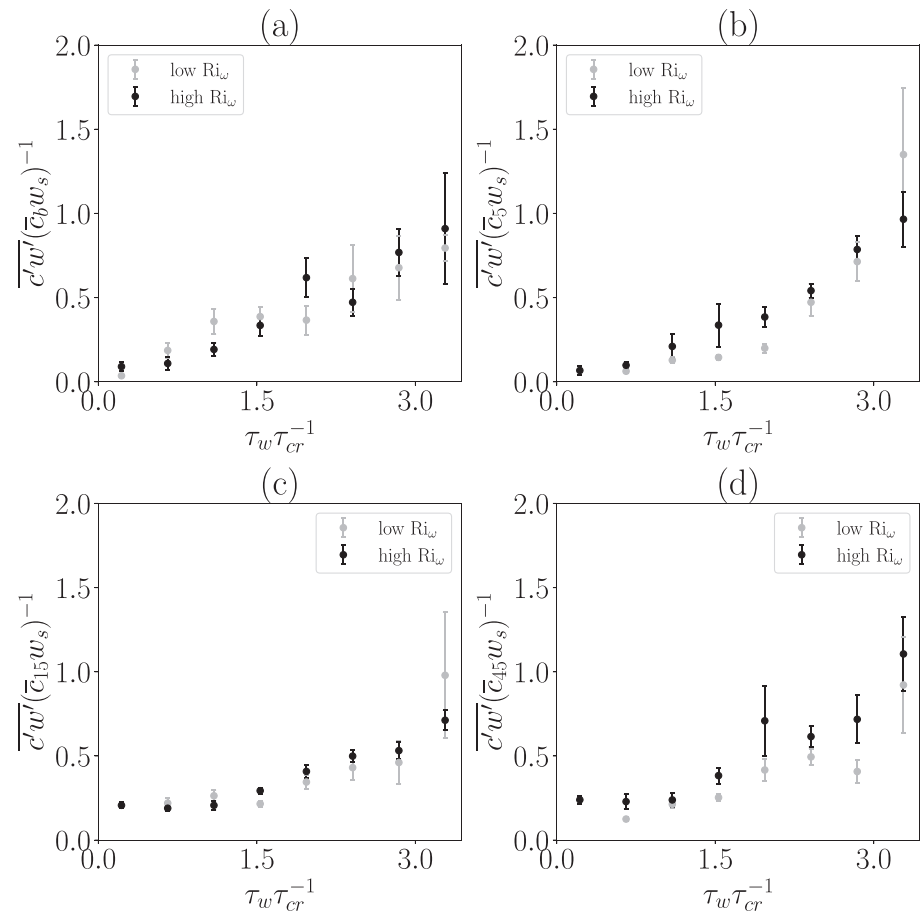
Figure 8. Turbulent sediment flux measured by the (a) Vectrino at 1 mm above the canopy top, nondimensionalized by $c_b w_s$, and by the ADVs at (b) 5 cmab and normalized by $c_5 w_s$, (c) 15 cmab and normalized by $c_{15} w_s$, and (d) 45 cmab and normalized by $c_{45} w_s$. Data are shown for both the weak stratification (gray dots) and strong stratification (black dots) cases, and bin averaged by the wave shear stress, τ_w (Equation 6), normalized by the critical shear stress, τ_{cr}. Error bars denote the standard error on the bin averaging.

Despite those effects, the overall decreases in the ADV Reynolds stress and TKE dissipation rate were substantial. This presents a significant difficulty for hydrodynamic models, because turbulence at the scale of the water depth, generally $\mathscr{O}(1-10)$ meters in estuaries, is affected by dynamics at the scale of the wave boundary layer, which is often $\mathscr{O}(1-10)$ millimeters. At present, it is computationally intractable to resolve that range of scales, which emphasizes the need for accurate parameterizations of sediment-induced stratification in sediment transport models.

4.5. Sediment Fluxes

Scalar fluxes are inherently linked to turbulent fluxes, meaning they can also be limited by stratification. In the case of sediment, the limiting stratification is set up once sufficient sediment has been eroded and strong enough SSC gradients are formed. To examine these dynamics, we separated $\overline{c'w'}(c_b w_s)^{-1}$ into strong and weak stratification burst periods by the same metric that we used for the drag coefficient in section 4.3. We then bin averaged the sediment fluxes by the wave shear stress, τ_w. We chose to nondimensionalize τ_w by the critical shear stress, τ_{cr}, obtained from our SEDflume erosion study, which indicated a critical shear stress of $\tau_{cr} = 0.18$ Pa at the top of the sediment core, that is, the bed. Sediment flux values more than three standard deviations from the median were again neglected.

Figure 8a shows the Vectrino turbulent sediment flux as a function of $\tau_w \tau_{cr}^{-1}$ for both strong and weak stratification conditions. Unlike the drag coefficient and turbulence statistics, here we see no significant

difference between the strongly and weakly stratified cases. The fluxes under each stratification condition increase steadily with wave shear stress beyond $\tau_w \tau_{cr}^{-1} \approx 1$.

We can also examine these trends in the ADV data. Figures 8b–8d show the normalized turbulent sediment flux at 5, 15, and 45 cmab, respectively, as a function of $\tau_w \tau_{cr}^{-1}$. Much like the Vectrino data, there is no significant difference between the strongly and weakly stratified cases. These trends are surprising given that both the Vectrino and ADV Reynolds stresses decreased with stratification (Figures 6 and 7); one would expect the sediment fluxes to follow suit. This could be explained by the increased SSC in the bottom boundary layer that accompanies stratification. Even if turbulent fluctuations (i.e., w') decrease, SSC fluctuations (c') could increase, leading to a relatively constant $\overline{c'w'}$. In other words, the flow may lose a source of momentum when the bottom boundary layer is stratified, but it gains a source of sediment. Therefore, the turbulent sediment flux is unaffected both near the bed and throughout the water column.

4.6. Model Comparisons

We can examine the practical implications of our results by analyzing them within the framework of the SG2000 stratified wave-current boundary layer model. Figure 9 shows the measured eddy viscosity (Equation 11), bin averaged by wave Reynolds number (Equation 8), and separated into strong and weak stratification regimes, similar to our analysis for the drag coefficient in Figure 5. When using the SG2000 stability parameter to define the strength of stratification (Figure 9a), there is no consistent, significant difference in the measured eddy viscosity between the strong and weak stratification cases. The eddy viscosity shows a stronger response to the measured gradient Richardson number (Figure 9b), though this effect is mostly seen in the highest Re_δ bins. The largest differences are seen in Figure 9c, where the strongly stratified eddy viscosity remains smaller than the weakly stratified eddy viscosity by approximately a factor of two across the entire range of Re_δ. This implies that Ri_ω is better suited to represent stratification in oscillatory boundary layer flows than the stability parameter in SG2000.

To understand why this may be the case, we note that the stability parameter can be recast in terms of the flux Richardson number, Ri_f, using

$$\frac{z}{L} = \frac{K}{K_{strat}} \mathrm{Ri}_f, \tag{16}$$

where

$$\mathrm{Ri}_f = \frac{K_{strat}}{u_{*cw}^4} \frac{g}{\rho} \overline{\rho' w'}. \tag{17}$$

There is no universally agreed upon way to relate Ri_f to Ri_g, but a commonly used parameterization suggested by Mellor and Yamada (1982) is

$$\mathrm{Ri}_f = 0.725 \left[\mathrm{Ri}_g + 0.186 - \left(\mathrm{Ri}_g^2 - 0.316 \mathrm{Ri}_g + 0.0346 \right)^{1/2} \right]. \tag{18}$$

Therefore, the stability parameter is proportional to the gradient Richardson number, which as we discussed in section 4.2, is more appropriate for steady shear flows where the stratification is an independent parameter.

There is a major caveat to this analysis: Even if Ri_ω is a more appropriate dimensionless parameter for examining stratification in oscillatory boundary layers, it is not helpful from a modeling standpoint if N is unknown. We were unable to find an expression for N in terms of independent flow and sediment variables (discussed in section 4.2), but Ri_ω could be defined in a similar way to the stability parameter, that is, in terms of c and K,

$$\mathrm{Ri}_\omega = -\frac{g}{\rho_0} \left(\frac{s-1}{s} \right) \frac{w_s \overline{c}}{K} \omega^{-2}. \tag{19}$$

After assuming a relationship between Ri_ω and K_{strat} (analogous to Equation 9), this new stratification parameter could be updated iteratively in a model until the associated velocity and SSC profiles converge, as in
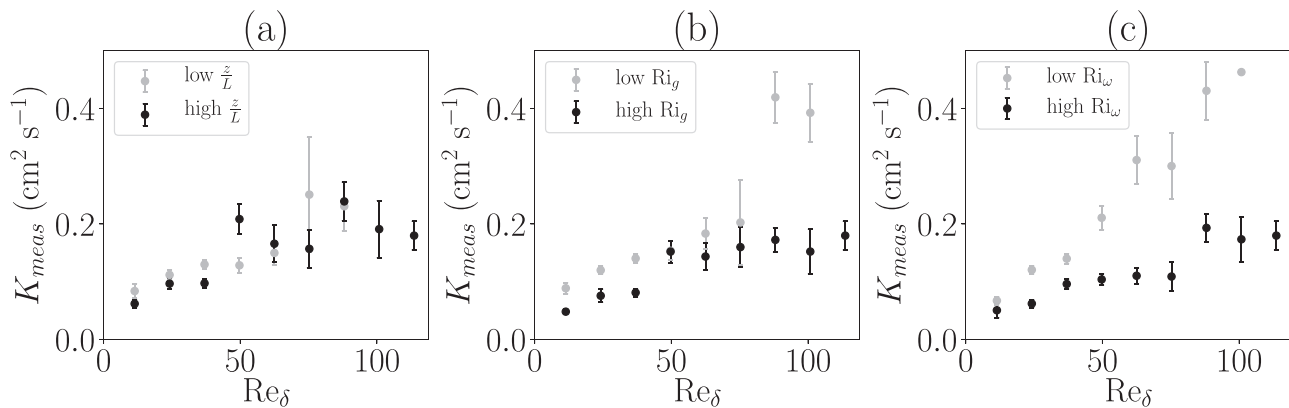
Figure 9. The measured eddy viscosity (Equation 11) plotted against the wave Reynolds number (Equation 8) and separated into weak stratification cases (gray dots) and strong stratification cases (black dots) using (a) the SG2000 stability parameter (Equation 10), (b) the gradient Richardson number (Equation 13), and (c) the wave frequency Richardson number, Ri_ω (Equation 14).

the SG2000 solution procedure. While it is outside the scope of this paper to develop and validate such a model, we hope that the results shown here will motivate future work in that direction.

5. Conclusions

We presented results from a field campaign studying the effects of sediment-induced stratification on the mean and turbulent boundary layer properties of a shallow, wave- and current-driven flow. Using high-resolution current velocity measurements obtained from acoustic instrumentation, we calculated the friction velocity to examine mean drag and turbulence statistics such as Reynolds stress, TKE dissipation, and the turbulent sediment flux. Each of these variables was examined across a range of wave and stratification conditions. Generally, we found that stratification can decrease the drag felt by the mean flow, which is likely caused by stratification-induced suppression of near-bed turbulent fluxes and TKE dissipation. This drag reduction may counteract wave-induced drag increases for weak to moderate wave conditions, a significant result for parameterizing drag in hydrodynamic and sediment transport models. Our analysis also suggests that erosion, parameterized through the turbulent sediment flux, may not require modification in stratified conditions.

The interplay among waves, turbulence, and stratification in the bottom boundary layer is complex, and feedback effects make it difficult to isolate the impact of one mechanism from another on the hydrodynamic response (e.g., in terms of bottom drag). This study measured bottom boundary layer processes in situ with excellent vertical spatial resolution. Our deployment resulted in over 2 weeks of hourly data, yet we were limited in our analysis by a relatively small number of measurement burst periods. Ideally, we would be able to separate our drag and sediment flux measurements into finer ranges of stratification conditions, rather than simply strong and weak as we did in Figures , 5, 8, and 9. Such an analysis would require more data, emphasizing the need for long-term field studies of sediment-induced stratification and laboratory studies in combined wave-current flumes over cohesive sediment beds.

Laboratory studies would also be helpful in validating improved wave-current boundary layer models. Our analysis in section 4.6 showed that Ri_ω may be more appropriate for quantifying the magnitude of density stratification in a wavy flow than the commonly used stability parameter, $\frac{z}{L}$. This is not entirely surprising, as the stability parameter theory was developed for atmospheric boundary layers (Monin & Obukhov, 1954) rather than estuarine wave-current boundary layers. A model based on our stratification parameter would not be a major departure from existing theories, since Ri_ω is merely a Richardson number based on the wave frequency rather than the mean current shear. Incorporating this modification into a stratified wave-current boundary layer model could lead to significant improvements in the predictive capabilities of sediment transport models.

Data Availability Statement

All data used in this paper are available at https://purl.stanford.edu/wv787xr0534.

References

Abarbanel, H. D. I., Holm, D. D., Marsden, J. E., & Ratiu, T. (1984). Richardson number criterion for the nonlinear stability of three-dimensional stratified flow. *Physical Review Letters*, *52*(26), 2352.

Agrawal, Y. C., & Pottsmith, H. C. (1994). Laser diffraction particle sizing in STRESS. *Continental Shelf Research*, *14*(10-11), 1101–1121.

Brand, A., Lacy, J., Hsu, K., Hoover, D., Gladding, S., & Stacey, M. (2010). Wind-enhanced resuspension in the shallow waters of south San Francisco Bay: Mechanisms and potential implications for cohesive sediment transport. *Journal of Geophysical Research*, *115*, C11024. https://doi.org/10.1029/2010JC006172

Bricker, J. D., Inagaki, S., & Monismith, S. G. (2005). Bed drag coefficient variability under wind waves in a tidal estuary. *Journal of Hydraulic Engineering*, *131*(6), 497–508.

Bricker, J. D., & Monismith, S. G. (2007). Spectral wave-turbulence decomposition. *Journal of Atmospheric and Oceanic Technology*, *24*(8), 1479–1487.

Cantero, M. I., Balachandar, S., Cantelli, A., Pirmez, C., & Parker, G. (2009a). Turbidity current with a roof: Direct numerical simulation of self-stratified turbulent channel flow driven by suspended sediment. *Journal of Geophysical Research: Oceans*, *114*(C3).

Cantero, M. I., Balachandar, S., Cantelli, A., Pirmez, C., & Parker, G. (2009b). Turbidity current with a roof: Direct numerical simulation of self-stratified turbulent channel flow driven by suspended sediment. *Journal of Geophysical Research*, *114*, C03008. https://doi.org/10.1029/2008JC004978

Cantero, M. I., Balachandar, S., & Parker, G. (2009). Direct numerical simulation of stratification effects in a sediment-laden turbulent channel flow. *Journal of Turbulence*, *10*, N27.

Chou, Y.-J., Nelson, K. S., Holleman, R. C., Fringer, O. B., Stacey, M. T., Lacy, J. R., et al. (2018). Three-dimensional modeling of fine sediment transport by waves and currents in a shallow estuary. *Journal of Geophysical Research: Oceans*, *123*, 4177–4199. https://doi.org/10.1029/2017JC013064

Craig, R. G. A., Loadman, C., Clement, B., Rusello, P. J., & Siegel, E. (2011). Characterization and testing of a new bistatic profiling acoustic Doppler velocimeter: The Vectrino-II. In *2011 IEEE/OES 10th Current, Waves and Turbulence Measurements (CWTM)* (pp. 246–252).

Deltares (2019). Delft3D-Flow: Simulation of multi-dimensional hydrodynamic flows and transport phenomena, including sediments.

Egan, G., Cowherd, M., Fringer, O., & Monismith, S. (2019). Observations of near-bed shear stress in a shallow, wave-and current-driven flow. *Journal of Geophysical Research: Oceans*, *124*, 6323–6344. https://doi.org/10.1029/2019JC015165

Feddersen, F., Trowbridge, J. H., & Williams III, A. J. (2007). Vertical structure of dissipation in the nearshore. *Journal of Physical Oceanography*, *37*(7), 1764–1777.

Fong, D. A., Monismith, S. G., Stacey, M. T., & Burau, J. R. (2009). Turbulent stresses and secondary currents in a tidal-forced channel with significant curvature and asymmetric bed forms. *Journal of Hydraulic Engineering*, *135*(3), 198–208.

Friedrichs, C. T., Wright, L. D., Hepworth, D. A., & Kim, S. C. (2000). Bottom-boundary-layer processes associated with fine sediment accumulation in coastal seas and bays. *Continental Shelf Research*, *20*(7), 807–841.

Glenn, S. M., & Grant, W. D. (1987). A suspended sediment stratification correction for combined wave and current flows. *Journal of Geophysical Research*, *92*(C8), 8244–8264.

Grant, W. D., & Madsen, O. S. (1979). Combined wave and current interaction with a rough bottom. *Journal of Geophysical Research*, *84*(C4), 1797–1808.

Grant, W. D., & Madsen, O. S. (1986). The continental-shelf bottom boundary layer. *Annual Review of Fluid Mechanics*, *18*(1), 265–305.

Gross, E. S., Koseff, J. R., & Monismith, S. G. (1999). Three-dimensional salinity simulations of south San Francisco Bay. *Journal of Hydraulic Engineering*, *125*(11), 1199–1209.

Hooshmand, A., Horner-Devine, A. R., & Lamb, M. P. (2015). Structure of turbulence and sediment stratification in wave-supported mud layers. *Journal of Geophysical Research: Oceans*, *120*, 2430–2448. https://doi.org/10.1002/2014JC010231

Howard, L. N. (1961). Note on a paper of John W. Miles. *Journal of Fluid Mechanics*, *10*(4), 509–512.

Jensen, B. L., Sumer, B. M., & Fredsøe, J. (1989). Turbulent oscillatory boundary layers at high Reynolds numbers. *Journal of Fluid Mechanics*, *206*, 265–297.

Jonsson, I. G. (1967). Wave boundary layers and friction factors. In *Coastal engineering 1966* (pp. 127–148). Washington, DC.

Kamphuis, J. W. (1975). Friction factor under oscillatory waves. *Journal of the Waterways, Harbors and Coastal Engineering Division*, ASCE *101*(2), 135–144.

Lacy, J. R., & MacVean, L. J. (2016). Wave attenuation in the shallows of San Francisco Bay. *Coastal Engineering*, *114*, 159–168.

Li, M. Z. (2000). Boundary layer dynamics and drag reduction in flows of high cohesive sediment suspensions. *Sedimentology*, *47*(1), 71–86.

Lohrmann, A. (2001). Monitoring sediment concentration with acoustic backscattering instruments. *Nortek Technical Note*, *3*, 1–5.

MacVean, L. J., & Lacy, J. (2014). Interactions between waves, sediment, and turbulence on a shallow estuarine mudflat. *Journal of Geophysical Research: Oceans*, *119*, 1534–1553. https://doi.org/10.1002/2013JC009477

Manning, A. J., Bass, S. J., & Dyer, K. R. (2006). Floc properties in the turbidity maximum of a mesotidal estuary during neap and spring tidal conditions. *Marine Geology*, *235*(1-4), 193–211.

Manning, A. J., Friend, P. L., Prowse, N., & Amos, C. L. (2007). Preliminary findings from a study of Medway Estuary (UK) natural mud floc properties using a laboratory mini-flume and the LabSFLOC system. *Continental Shelf Research*, *BIOFLOW SI*, 1080–1095.

McNeil, J., Taylor, C., & Lick, W. (1996). Measurements of erosion of undisturbed bottom sediments with depth. *Journal of Hydraulic Engineering*, *122*(6), 316–324.

Mehta, A. J., & Partheniades, E. (1982). Resuspension of deposited cohesive sediment beds. In *Coastal Engineering 1982* (pp. 1569–1588).

Mellor, G. L., & Yamada, T. (1982). Development of a turbulence closure model for geophysical fluid problems. *Reviews of Geophysics*, *20*(4), 851–875.

Miles, J. W. (1961). On the stability of heterogeneous shear flows. *Journal of Fluid Mechanics*, *10*(4), 496–508.

Monin, A. S., & Obukhov, A. M. (1954). Basic laws of turbulent mixing in the surface layer of the atmosphere. *Contributions of the Geophysical Institute of the Academy of Sciences, USSR*, *151*, 163–187.

Munk, W. H. (1948). Note on the theory of the thermocline. *Journal of Marine Research*, *7*, 276–295.

Nelson, K. S. (2018). Simulating suspended sediment dynamics in shallow-water wave-and current-driven environments (Ph.D. Thesis), Stanford University.

Nelson, K. S., & Fringer, O. B. (2018). Sediment dynamics in wind wave-dominated shallow-water environments. *Journal of Geophysical Research: Oceans*, *123*, 6996–7015. https://doi.org/10.1029/2018JC013894

Nielsen, P. (1992). *Coastal bottom boundary layers and sediment transport* (Vol. 4). World Scientific Publishing Company.

Ozdemir, C. E., Hsu, T.-J., & Balachandar, S. (2010). A numerical investigation of fine particle laden flow in an oscillatory channel: The role of particle-induced density stratification. *Journal of Fluid Mechanics*, *665*, 1–45.

Sanford, L. P., & Maa, J. P. (2001). A unified erosion formulation for fine sediments. *Marine Geology*, *179*(1), 9–23.

Smith, J. D., & McLean, S. R. (1977). Boundary layer adjustments to bottom topography and suspended sediment. *Elsevier Oceanography Series* (Vol. 19, pp. 123–151). Elsevier.

Stokes, G. G. (1851). *On the effect of the internal friction of fluids on the motion of pendulums* (Vol. 9). Pitt Press Cambridge.

Styles, R., & Glenn, S. M. (2000). Modeling stratified wave and current bottom boundary layers on the continental shelf. *Journal of Geophysical Research*, *105*(C10), 24,119–24,139.

Thomas, R. E., Schindfessel, L., McLelland, S. J., Creëlle, S., & De Mulder, T. (2017). Bias in mean velocities and noise in variances and covariances measured using a multistatic acoustic profiler: The Nortek Vectrino profiler. *Measurement Science and Technology*, *28*(7), 075302.

Villaret, C., & Trowbridge, J. H. (1991). Effects of stratification by suspended sediments on turbulent shear flows. *Journal of Geophysical Research*, *96*(C6), 10,659–10,680.

Warner, J. C., Sherwood, C. R., Signell, R. P., Harris, C. K., & Arango, H. G. (2008). Development of a three-dimensional, regional, coupled wave, current, and sediment-transport model. *Computers & Geosciences*, *34*(10), 1284–1306.

Erratum

In order to calculate wave shear stress, τ_w, we used Equation 6, which is a function of the friction factor defined in Equation 7 of the original manuscript. This choice was based on the wave Reynolds number regime, which indicated that the wave boundary layer was laminar. However, this classification was based on a form of the wave Reynolds number that is inconsistent with the cited literature (Jonsson, 1967). Throughout the manuscript, we use the wave Reynolds number defined as

$$Re_\delta = \frac{u_b \delta_w}{\nu},$$

where u_b is the bottom wave-orbital velocity, δ_w is the Stokes wave boundary layer thickness, and ν is the kinematic viscosity. This corresponds to the variable "Re" in the Jonsson paper cited above. It is a valid and widely-used wave Reynolds number, and to avoid further changes to the manuscript we will retain its use as our nondimensional number of choice to characterize wave strength. However, the delineation of the boundary layer into a laminar and turbulent regime should actually be defined in terms of an alternative wave Reynolds number,

$$Re_w = \frac{u_b a_b}{\nu} = \frac{a_b^2 \omega}{\nu},$$

where a_b is the bottom wave-orbital excursion amplitude. This corresponds to the variable "RE" in the Jonsson paper. Using this proper formulation, we found that our wave boundary layer was indeed turbulent. Therefore, the proper friction factor to use was not

$$f_w = 2\,Re_\delta^{-0.5}$$

as originally written, but rather

$$f_w = \exp\left(5.213\left(\frac{k_b}{a_b}\right)^{0.194} - 5.977\right).$$

where k_b is the physical bottom roughness (Nielsen, 1992).

The impact of this change was minimal, as the wave shear stress only appeared in Figure 8. After updating Figure 8 using the proper friction factor, we found that the trends were effectively identical, albeit with the wave shear stress shifted to lower values.

These changes have been implemented, and this may be considered the official version of record.